Monthly Notices of the ROYAL ASTRONOMICAL SOCIETY

MNRAS **528,** 6119–6128 (2024) https://doi.org/10.1093/mnras/stae355
Advance Access publication 2024 February 2

# Effective viscosity, resistivity, and Reynolds number in weakly collisional plasma turbulence

Yan Yang,[1]★ William H. Matthaeus,[1] Sean Oughton,[2] Riddhi Bandyopadhyay,[3] Francesco Pecora,[1] Tulasi N. Parashar,[4] Vadim Roytershteyn,[5] Alexandros Chasapis[6] and Michael A. Shay[1]

[1]*Department of Physics and Astronomy, University of Delaware, Newark, DE 19716, USA*
[2]*Department of Mathematics, University of Waikato, Hamilton 3240, New Zealand*
[3]*Department of Astrophysical Sciences, Princeton University, Princeton, NJ 08544, USA*
[4]*School of Chemical and Physical Sciences, Victoria University of Wellington, Wellington 6012, New Zealand*
[5]*Space Science Institute, Boulder, CO 80301, USA*
[6]*Laboratory for Atmospheric and Space Physics, University of Colorado Boulder, Boulder, CO 80309, USA*

Accepted 2024 January 29. Received 2023 December 31; in original form 2023 August 30

## ABSTRACT

We examine dissipation and energy conversion in weakly collisional plasma turbulence, employing *in situ* observations from the Magnetospheric Multiscale mission and kinetic particle-in-cell simulations of proton–electron plasma. A previous result indicated the presence of viscous-like and resistive-like scaling of average energy conversion rates – analogous to scalings characteristic of collisional systems. This allows for extraction of collisional-like coefficients of *effective* viscosity and resistivity, and thus also determination of effective Reynolds numbers based on these coefficients. The effective Reynolds number, as a measure of the available bandwidth for turbulence to populate various scales, links turbulence macroscale properties with kinetic plasma properties in a novel way.

**Key words:** plasmas – turbulence – Sun: heliosphere – solar wind.

## 1 INTRODUCTION

Energy dissipation in fluids and plasmas may be effectively defined as the conversion process by which macroscopic reservoirs of energy are transformed into heat. Mechanisms of energy dissipation for weakly collisional or collisionless plasma are of central importance for addressing long-standing fundamental problems in space physics and astrophysics. These include, for example, the acceleration of energetic particles and the heating of the solar corona and solar wind. In collisional cases, the (viscous and resistive) dissipation is expressed in a simple form in terms of viscosity, resistivity, and spatial gradients of the velocity and magnetic fields. However, space plasmas frequently reside in (nearly) collisionless regimes, where the dissipation mechanisms are not well understood. For example, in one of the most well-studied space plasmas, the solar wind (Bruno & Carbone 2013), the collision length is of the order of 1 au and collisions are typically too weak to establish a local equilibrium (Maxwellian particle distribution; Marsch 2006; Verniero et al. 2020). In such cases, the classical collisional approach becomes generally inapplicable, as do standard closures that describe dissipation in terms of fluid-scale variables and viscosity and resistivity.

Lacking the standard collisional closures, studies of plasma turbulence have shown increasing interest in quantifying collisionless dissipation. Investigations of collisionless dissipation have often considered one or more of the following three aspects:

(i) *Dissipation mechanisms*: Collisionless dissipation has often been described in terms of specific mechanisms such as magnetic reconnection (Retinò et al. 2007), wave–particle interaction (Markovskii et al. 2006; Howes et al. 2008; Chandran et al. 2010), and turbulence-driven intermittency (Dmitruk, Matthaeus & Seenu 2004; Parashar et al. 2011). Identification of such processes affords specific physical insight. If all possible mechanisms and their relative contributions can be identified, a full understanding of the dissipation physics may be achievable.

(ii) *Turbulence cascade*: The picture of turbulence cascade describes energy transfer across scales from an energy-containing range, through an inertial range, and into a (small-scale) dissipation range. Different dissipation proxies based on the turbulence cascade process have been adopted to estimate the dissipation rate. At energy-containing scales, the global decay rate of energy is controlled by the von Kármán decay law (de Kármán & Howarth 1938; Hossain et al. 1995; Wan et al. 2012; Zank et al. 2017). At inertial-range scales, the Yaglom relation (Politano & Pouquet 1998; Sorriso-Valvo et al. 2007; Hadid, Sahraoui & Galtier 2017; Andrés et al. 2019; Banerjee & Andrés 2020) has been adapted to estimate the energy transfer rate. Hellinger et al. (2022) extended this approach into the kinetic range by empirically including pressure–strain interaction effects in the kinetic range.

(iii) *Energy conversion channels*: Yet another approach to understand dissipation is to trace the flow of energy and examine energy conversion between different forms. Temperature enhancement implies increase of thermal energy and to specifically track thermal energy production requires quantification of energy supplies from

★ E-mail: yanyang@udel.edu

energy reservoirs for each species. Two widely invoked classes of conversion are the electric work on particles for species $\alpha$, $\boldsymbol{J}_\alpha \cdot \boldsymbol{E}$ (Zenitani et al. 2011), and the pressure–strain interaction for species $\alpha$, $-(\boldsymbol{P}_\alpha \cdot \nabla) \cdot \boldsymbol{u}_\alpha$ (e.g. Chiuderi & Velli 2015; Del Sarto, Pegoraro & Califano 2016; Yang et al. 2017a, b; Barbhuiya & Cassak 2022; Cassak & Barbhuiya 2022; Cassak, Barbhuiya & Weldon 2022).(We employ a familiar plasma physics notation with full definitions given in Section 2.) These channels play different roles: the electric work measures the release of electromagnetic energy, while the pressure–strain interaction measures the increase of thermal energy.

Collisional and collisionless dissipation obviously differ from each other, but they also share similarities. For example, in both cases, conversion of energy between different forms can be quantified in terms of pressure work and electric work.

In collisional cases, however, these two channels can be further approximated as viscous dissipation via velocity gradients and resistive dissipation via electric current density (i.e. magnetic field gradients), which will be discussed in detail in Section 2. On the other hand, investigations using *in situ* spacecraft data (Chasapis et al. 2018; Bandyopadhyay et al. 2020a) and numerical simulations (Wan et al. 2016; Yang et al. 2017a) support a novel and less obvious idea, namely that collision*less* dissipation is also in direct association with velocity strain rate and electric current density (Bandyopadhyay et al. 2023). More specifically, by quantifying collisionless dissipation by the electric work $\boldsymbol{J}_\alpha \cdot \boldsymbol{E}$ and the pressure–strain interaction $-(\boldsymbol{P}_\alpha \cdot \nabla) \cdot \boldsymbol{u}_\alpha$, these are seen to be well correlated with, respectively, squared electric current density and squared velocity strain rate. This association stands in direct analogy to the resistive and viscous dissipation in collisional plasmas. It is natural then to inquire more deeply into the behaviour of collisionless dissipation and its similarities with collisional dissipation.

Initial steps in this direction have shown two findings. First, the global average of electric work conditioned on electric current density scales as $J^2$, i.e. the square of the current density (Wan et al. 2016; Chasapis et al. 2018). Secondly, there is a similar scaling of pressure work with respect to $D^2 = D_{ij}D_{ij}$, where $D_{ij}$ is the traceless velocity strain rate tensor (Bandyopadhyay et al. 2023). These results provide strong evidence supporting the concept of collisional-*like* dissipation in collisionless plasmas, and, moreover, allow a novel estimation of effective viscosity and resistivity, which is then further applied to define *effective Reynolds numbers*.

Since the classical closures of viscosity and resistivity are inapplicable to collisionless plasmas, one might suspect that various features of classical turbulence theory might not be applicable, in particular regarding dissipative processes and the several length-scales and dimensionless numbers related to dissipation. Even the notion of Reynolds number (Re) – which in the hydrodynamic sense is the ratio of the strengths of non-linear and viscous effects – needs to be considered with caution in the absence of viscosity and resistivity. On the other hand, a point of encouragement is that wavenumber spectra in large collisionless plasmas such as the solar wind (Bruno & Carbone 2013) often exhibit a Kolmogorov-like power-law energy spectrum (Coleman 1968) that extends from a correlation scale (Matthaeus et al. 2005) to smaller kinetic scales (Leamon et al. 1998), below which the spectrum steepens. Between these scales, the power-law inertial range is expected to span a larger range when the Reynolds number is greater, by analogy with hydrodynamics.

To achieve physically motivated generalizations of Re in the collisionless case, previous studies have adopted various definitions of effective Reynolds number, often related to the ratio of an outer scale to an inner scale. For example,

$$\mathrm{Re} \approx \left(\frac{\lambda_c}{\lambda_d}\right)^{4/3} \quad \text{or} \quad \mathrm{Re} \approx \left(\frac{\lambda_c}{\lambda_\mathrm{T}}\right)^{2}, \tag{1}$$

where $\lambda_c$ is the correlation length, $\lambda_d$ is a dissipation scale, and $\lambda_\mathrm{T}$ is the Taylor microscale (Batchelor 1970; Pope 2000). For a weakly collisional plasma, such as the solar wind, the dissipation scale can be presumed to be the ion inertial length $d_\mathrm{p}$ or the ion thermal gyroradius (Verma 1996; Parashar, Cuesta & Matthaeus 2019; Cuesta et al. 2022), given that the inertial-range spectrum terminates (and then steepens) near these scales (Leamon et al. 1998; Smith et al. 2006; Matthaeus et al. 2008; Chen et al. 2014). Another scale related to dissipation is the Taylor microscale $\lambda_\mathrm{T}$. This has been measured in the solar wind and then used to estimate effective Reynolds number for that system (Matthaeus et al. 2005, 2008; Chuychai et al. 2014; Bandyopadhyay et al. 2020b; Phillips, Bandyopadhyay & McComas 2022; Wrench et al. 2023). Note that both of the empirical determinations of effective Reynolds number given by equation (1) depend on the appropriate estimates of inner scales. Herein, we adopt a different approach that avoids any need to estimate inner scales. In a novel examination of the putative connection between collisional and collisionless dissipation, we explore specific evaluations of effective viscosity, resistivity, and Reynolds number from 2.5-dimensional (2.5D) and three-dimensional (3D) kinetic particle-in-cell (PIC) simulations and *in situ* observations from the Magnetospheric Multiscale (MMS) mission.

## 2 THEORETICAL BACKGROUND

We are concerned with observed phenomena related to energy conversion processes. Herein, we focus on the bulk flow energy, electromagnetic energy, thermal energy, and the conversion and dissipation channels that link them. For consistency in the contexts of observational and simulation data, all quantities will be expressed in International System (SI) units throughout the paper.

### 2.1 Collisional cases

We start with the simplest one-fluid magnetohydrodynamic (MHD) model. The momentum and magnetic induction equations read

$$\rho \frac{\partial \boldsymbol{u}}{\partial t} + \rho \boldsymbol{u} \cdot \nabla \boldsymbol{u} = -\nabla p - \nabla \cdot \boldsymbol{\Pi} + \boldsymbol{J} \times \boldsymbol{B}, \tag{2}$$

$$\frac{\partial \boldsymbol{B}}{\partial t} - \nabla \times (\boldsymbol{u} \times \boldsymbol{B}) = \eta \nabla^2 \boldsymbol{B}, \tag{3}$$

where $\Pi_{ij} = -\mu\left(\partial_i u_j + \partial_j u_i\right) + \frac{2}{3}\mu(\nabla \cdot \boldsymbol{u})\delta_{ij}$ is the viscous stress tensor, $\boldsymbol{J} = \frac{1}{\mu_0}\nabla \times \boldsymbol{B}$ is the electric current density, $\mu$ is the dynamic viscosity, $\eta$ is the magnetic diffusivity, and $\mu_0 = 4\pi \times 10^{-7}\ \mathrm{H\,m^{-1}}$ is the magnetic permeability of free space (also known as vacuum permeability).

Based on equations (2) and (3), one readily obtains the collisional dissipation rates of bulk flow energy density ($E_u = \frac{1}{2}\rho \boldsymbol{u}^2$) and magnetic energy density ($E_b = \frac{1}{2\mu_0}\boldsymbol{B}^2$). These can be expressed in terms of the coefficients of dynamic viscosity ($\mu$) and electrical resistivity ($1/\sigma \equiv \mu_0\eta$), and particular pieces of the velocity gradient and magnetic gradient tensors:

$$D_\mu = 2\mu D^2, \tag{4}$$

$$D_\eta = \frac{1}{\sigma} J^2. \tag{5}$$

Here, $D_{ij} = \frac{1}{2}(\partial_i u_j + \partial_j u_i) - \frac{1}{3}(\nabla \cdot \boldsymbol{u})\delta_{ij}$ is the traceless strain rate tensor, with $D^2 = D_{ij}D_{ij}$ the second invariant of $D_{ij}$ and equal to the sum of the squares of the eigenvalues of $D_{ij}$.

As is well known, the viscous dissipation in equation (4) and the resistive dissipation in equation (5) actually originate from the *closures* of the deviatoric pressure tensor $\boldsymbol{\Pi}$ and the electric field $\boldsymbol{E}$ that hold in the presence of frequent collisions.

These can be derived by kinetic methods (Chapman & Cowling 1939; Kaufman 1960; Marshall 1960; Braginskii 1965), where an approximate solution for the Boltzmann equation is first obtained in terms of macroscopic variables (like density, velocity, and temperature) and the pressure tensor [the second-order moment of the velocity distribution function (VDF)] is then also expressed in terms of macroscopic variables. The closure of the electric field can be derived using Ohm's law. In outline, the procedure is as follows: (i) In the presence of frequent collisions, it can be shown that no matter what the initial conditions are the VDF $f$ must approach a Maxwellian $f_0$ in a time of the order of the mean time between collisions (Chapman & Cowling 1939). (ii) The VDF $f$ is assumed to be approximately a Maxwellian $f_0$ and higher order terms ($f_1$, $f_2$, $\cdots$) are introduced as small corrections or perturbations on the Maxwellian distribution function, $f = f_0 + f_1 + f_2 + \cdots$. (iii) Retaining only the first-order correction $f_1$ can give rise to the closures of the electric field, $\boldsymbol{E} + \boldsymbol{u} \times \boldsymbol{B} = \boldsymbol{J}/\sigma$, and the deviatoric pressure tensor, $\Pi_{ij} = -2\mu D_{ij}$, which then leads to the collisional dissipation forms (equations 4 and 5).

To prescribe the applicability of the collisional approximation, we should keep in mind its requirement: *Even though the collisional dissipation provides a simple representation of dissipation in terms of the viscosity and resistivity, in all standard cases it applies only when the local distribution is very close to a Maxwellian due to particle collisions.*

### 2.2 Collisionless cases

The time evolution of energies can be derived using the first three moments of the Boltzmann equation, in conjunction with the Maxwell equations. One obtains (Braginskii 1965; Chiuderi & Velli 2015; Yang et al. 2017a, b)

$$\partial_t \mathcal{E}_\alpha^f + \nabla \cdot \left(\mathcal{E}_\alpha^f \boldsymbol{u}_\alpha + \boldsymbol{P}_\alpha \cdot \boldsymbol{u}_\alpha\right) = (\boldsymbol{P}_\alpha \cdot \nabla) \cdot \boldsymbol{u}_\alpha + \boldsymbol{J}_\alpha \cdot \boldsymbol{E}, \tag{6}$$

$$\partial_t \mathcal{E}_\alpha^{\rm th} + \nabla \cdot \left(\mathcal{E}_\alpha^{\rm th} \boldsymbol{u}_\alpha + \boldsymbol{h}_\alpha\right) = -(\boldsymbol{P}_\alpha \cdot \nabla) \cdot \boldsymbol{u}_\alpha, \tag{7}$$

$$\partial_t \mathcal{E}^m + \nabla \cdot \left(\boldsymbol{E} \times \frac{\boldsymbol{B}}{\mu_0}\right) = -\boldsymbol{J} \cdot \boldsymbol{E}, \tag{8}$$

where the subscript $\alpha = e, p$ represents the particle species (electrons and protons). Here, $\mathcal{E}^m = \frac{1}{2}\left(\epsilon_0 \boldsymbol{E}^2 + \boldsymbol{B}^2/\mu_0\right)$ is the electromagnetic energy density, with $\boldsymbol{E}$ and $\boldsymbol{B}$ the electric and magnetic fields, respectively; $\mathcal{E}_\alpha^f = \frac{1}{2}\rho_\alpha \boldsymbol{u}_\alpha^2$ is the bulk flow energy density for species $\alpha$, with mass density $\rho_\alpha$ and bulk flow velocity $\boldsymbol{u}_\alpha$; $\mathcal{E}_\alpha^{\rm th} = \frac{1}{2} m_\alpha \int_v (\boldsymbol{v} - \boldsymbol{u}_\alpha) \cdot (\boldsymbol{v} - \boldsymbol{u}_\alpha) f_\alpha \, {\rm d}^3 v$ is the thermal energy, with mass $m_\alpha$ and VDF $f_\alpha(\boldsymbol{x}, \boldsymbol{v})$; $\boldsymbol{P}_\alpha$ is the pressure tensor; $\boldsymbol{h}_\alpha$ is the heat flux vector; $\boldsymbol{J} = \sum_\alpha \boldsymbol{J}_\alpha$ is the total electric current density with $\boldsymbol{J}_\alpha = n_\alpha q_\alpha \boldsymbol{u}_\alpha$ the electric current density of species $\alpha$; and $n_\alpha(\boldsymbol{x})$ and $q_\alpha$ are the number density and the charge of species $\alpha$, respectively. As we can see, the energy conversion between bulk flow and thermal is quantified by the pressure–strain interaction, $-(\boldsymbol{P}_\alpha \cdot \nabla) \cdot \boldsymbol{u}_\alpha$, while the energy conversion between bulk flow and electromagnetic is quantified by the electric work, $\boldsymbol{J} \cdot \boldsymbol{E}$. We emphasize that there are no $\boldsymbol{J}_\alpha$ terms in the thermal energy equation (7).

The basic assumption of collisional dissipation is that interparticle collisions are sufficiently strong to maintain a local equilibrium. In principle, this assumption is not valid in collisionless plasmas. Instead, the particle VDF often displays a distorted out-of-equilibrium shape characterized by non-Maxwellian features as observed in *in situ* data (e.g. Graham et al. 2017; Perri et al. 2020) and in numerical simulations (Servidio et al. 2012). Although at large scales collisionless plasma can be described by the (collisional) MHD model, spacecraft *in situ* measurements reveal complex features at kinetic scales. At these small scales, kinetic processes must take place. One widely accepted picture of solar wind fluctuations is that they are characterized by broadband energy spectra with several spectral breaks and spectral steepening at kinetic scales (Leamon et al. 1998; Alexandrova et al. 2009; Sahraoui et al. 2009; Kiyani, Osman & Chapman 2015). In particular, observations indicate that the degree of steepening of velocity and magnetic field spectra at kinetic scales is clearly dependent on the dissipation rate (Smith et al. 2006). Clearly, collisionless dissipation delves deeply into kinetic plasma processes.

### 2.3 Similarities between collisional and collisionless dissipation

Even though collisionless dissipation differs from collisional dissipation in important ways, studies also suggest that there are similarities between them. First, they are both organized in structured patterns and concentrated at, or near, coherent structures. Coherent structures form dynamically in MHD and plasma flows and are found to be of importance in heating; they include current sheets and vortices. According to the definition of collisional dissipation in equations (4) and (5), it should not be at all surprising to find that the collisional dissipation occurs with intense values at (and near) these structures. The physical quantities that are responsible for the conversion of energy in collisionless plasmas (see equations 6–8) are also found to exhibit the same kind of spatial localization (Retinò et al. 2007; Osman et al. 2011; Servidio et al. 2012; Franci et al. 2016; Parashar & Matthaeus 2016; Yang et al. 2017a). In this sense, both collisional and collisionless dissipation concentrate in structured patterns. Secondly, both sorts of dissipation are in direct association with velocity strain rate and electric current density. As we have already remarked, collisionless dissipation, as quantified by the electric work $\boldsymbol{J}_\alpha \cdot \boldsymbol{E}$ and the pressure–strain interaction $-(\boldsymbol{P}_\alpha \cdot \nabla) \cdot \boldsymbol{u}_\alpha$, is found to be in direct statistical association with $J^2$ and $D^2$ (Wan et al. 2016; Yang et al. 2017a; Chasapis et al. 2018; Bandyopadhyay et al. 2020a, 2023), and this scaling is strikingly analogous to the resistive and viscous dissipation that equations (4) and (5) represent. Meanwhile, existing work (Thompson 1961; Roberts & Taylor 1962; Macmahon 1965; Smolyakov 1998), including a finite Larmor radius correction to the ion pressure tensor, demonstrates a gyroviscous closure for the pressure tensor in the absence of particle collisions.

The aforementioned similarities between collisionless and collisional dissipation suggest that the scalings between collisional dissipation and flow gradients might remain valid for collisionless dissipation situations. The results presented herein provide further evidence for this hypothesis. In particular, our results (shown later) support the statistical relations

$$\langle -\Pi_{ij} D_{ij} | D \rangle \sim 2\mu D^2, \tag{9}$$

$$\langle \boldsymbol{J} \cdot \boldsymbol{E}' | J \rangle \sim \frac{1}{\sigma} J^2, \tag{10}$$

where $\Pi_{ij} = P_{ij} - p\delta_{ij}$ is the deviatoric pressure tensor, and $\boldsymbol{E}' = \boldsymbol{E} + \boldsymbol{u}_e \times \boldsymbol{B}$ is the electric field in the electron fluid frame. Here, $\langle -\Pi_{ij} D_{ij} | D \rangle$ is the average of the anisotropic part of the pressure–strain interaction conditioned on $D \equiv \sqrt{D_{ij} D_{ji}}$, and $\langle \boldsymbol{J} \cdot \boldsymbol{E}' | J \rangle$ is the average of the electric work in the electron fluid frame conditioned on the (local) current magnitude $J = |\boldsymbol{J}|$. If the scalings in equations (9) and (10) can be verified, they will permit an evaluation of effective values for dynamic viscosity $\mu$ and electrical resistivity $1/\sigma$, and thence for effective kinematic viscosity $\nu = \mu/\rho$, magnetic diffusivity $\eta = 1/(\sigma\mu_0)$, and Reynolds numbers.

We need to stress that we do not test a posteriori any analogous closures to collisional cases for the electric field and the pressure tensor in collisionless plasmas. Instead, we are trying a priori to find relations that hold between collisionless dissipation and the gradients of the flow so that they can be used in the construction of closures for collisionless dissipation. In this work, we focus on a global property – the global average of the collisionless dissipation – that suggests 'collisional-*like*' dissipation on average. However, upon checking local properties (not shown here), we find that the analogy between collisionless and collisional dissipation is far from pointwise accurate. The only similar studies in this direction, as far as we know, are Del Sarto et al. (2016) and Del Sarto & Pegoraro (2018), wherein the action of the strain tensor on the pressure tensor evolution is isolated. These authors found that even in an almost collisionless system, the shear flow and the pressure tensor anisotropy are strongly coupled and interact on fast time-scales. They further identified certain conditions, i.e. that the characteristic time of shear is negligible with respect to the cyclotron frequency, under which the deviatoric pressure tensor is proportional to the traceless strain rate tensor. Such considerations motivate future, more detailed, investigation of the local properties of $-\Pi_{ij} D_{ij}$ and $\boldsymbol{J} \cdot \boldsymbol{E}'$, which might allow extraction of non-uniform coefficients of effective viscosity and resistivity.

## 3 DATA

We present data from 2.5D and 3D fully kinetic PIC simulations and one long MMS burst-mode interval in the magnetosheath. In each case, the analysis leads to a determination of the associated (effective) resistivity and separate viscosities for electrons and protons.

The *2.5D PIC simulation* employs the P3D code (Zeiler et al. 2002), which has also been used in Yang et al. (2022, ) and Bandyopadhyay et al. (2023). Here, 2.5D means, as usual, that there are three components of dependent field vectors and a two-dimensional spatial grid, i.e. that the phase space coordinates are $(x, y, v_x, v_y, v_z)$. Normalization in P3D is largely 'proton based', with number density normalized to a reference value $n_r$, mass to proton mass $m_p$, charge to proton charge $e$, and magnetic field to a reference $B_r$. Length is normalized to the proton inertial length $d_p$, time to the proton cyclotron time $\omega_{cp}^{-1}$, and velocity to the consequent reference Alfvén speed $V_{Ar} = B_r/(\mu_0 m_p n_r)^{1/2}$.

The particular simulation we consider is performed in a square periodic domain of size $L = 150 d_p$, with $4096^2$ grid points and 3200 particles of each species per cell ($\sim 1.07 \times 10^{11}$ total particles). For numerical expediency, we employ artificially low values of the proton-to-electron mass ratio, $m_p/m_e = 25$, and the speed of light, $c = 15 V_{Ar}$. The run is a decaying initial value problem, starting with uniform densities and temperatures for both species. A uniform magnetic field, $B_0 = 1.0$, is directed out of the plane, and the initial proton and electron plasma $\beta$s are $\beta_p = \beta_e = 0.6$. The initial $\boldsymbol{v}$ and $\boldsymbol{b}$ fluctuations are transverse to $B_0$ ('Alfvén mode') and have Fourier modes with random phases for the wavenumber range $2 \leq |\boldsymbol{k}L/(2\pi)| \leq 4$. The initial normalized cross helicity $\sigma_c$ is negligible.

**Table 1.** 2.5D and 3D PIC simulation parameters in code units: domain size $L$; grid points in each direction $N$; proton-to-electron mass ratio $m_p/m_e$; guide magnetic field in $z$-direction $B_0$; initial magnetic fluctuation amplitude $\delta b$; plasma $\beta$; average number of particles of each species per grid cell *ppg*.

| Dimension | $L$ | $N$ | $m_p/m_e$ | $B_0\hat{z}$ | $\delta b/B_0$ | $\beta_p$ | ppg |
|---|---|---|---|---|---|---|---|
| 2.5D | $150 d_p$ | 4096 | 25 | 1.0 | 0.5 | 0.6 | 3200 |
| 3D | $296 d_e$ | 2048 | 50 | 0.5 | 1.0 | 0.25 | 150 |

The *3D simulation* (Roytershteyn, Karimabadi & Roberts 2015) is obtained using the VPIC code (Bowers et al. 2008), which was also used in Yang et al. (2022) and Bandyopadhyay et al. (2023). VPIC normalization differs significantly from that in P3D, being more electron based. Number density is normalized to a reference value $n_r$, mass to electron mass $m_e$, charge to proton charge $e$, length to the electron inertial length $d_e$, time to the electron plasma oscillation time $\omega_{pe}^{-1}$, velocity to the (true physical) speed of light $c$, and magnetic field to a reference $B_r = m_e c \omega_{pe}/e$.

The simulation of interest herein was performed in a cubic periodic domain of size $L = 296\, d_e$, with $2048^3$ grid points and 150 particles of each species per cell ($\sim 2.6 \times 10^{12}$ total particles). The proton-to-electron mass ratio is $m_p/m_e = 50$. Like the P3D run, this one is also a decaying initial value problem, starting with uniform density and temperature of protons and electrons. There is a uniform magnetic field $B_0 = 0.5$ in the out-of-plane $\hat{z}$ direction, and the proton and electron plasma $\beta$s are $\beta_p = \beta_e = 0.25$. The $\boldsymbol{v}$ and $\boldsymbol{b}$ fluctuations are initialized with two orthogonal polarizations and an overall power spectrum decaying as $k^{-1}$ for the wavenumber range $1 \leq |\boldsymbol{k}L/(2\pi)| \leq 7$ with equal power in each polarization. The initial $\boldsymbol{v}$ and $\boldsymbol{b}$ fluctuations are a mixture of Alfvénic and randomly phased perturbations. The initial normalized cross helicity is $\sigma_c \simeq 0.44$.

Key parameters for the 2.5D and 3D runs are given in Table 1. For both runs, we analyse statistics at a time shortly after that at which the maximum mean square current density occurs. Prior to analyses, we remove noise inherent in the PIC plasma algorithm via a low-pass Fourier filtering of the fields.

In addition to simulation data, we also analyse an interval of MMS spacecraft data. The MMS mission provides high time cadence and simultaneous multispacecraft measurements, typically in a tetrahedral formation, with small inter-spacecraft separations. The MMS spacecrafts sample the near-Earth plasma including the magnetosheath (Burch et al. 2016). The proton and electron 3D VDFs are available from the Fast Plasma Investigation (FPI) instrument (Pollock et al. 2016). One can then determine density, velocity, pressure tensor, and current density, with a time resolution of 150 ms for ions and 30 ms for electrons. The Flux-Gate Magnetometer (Russell et al. 2016) measures the vector magnetic field, and the Electric Field Double Probes (Ergun et al. 2016) measures the electric field. Herein, we employ a single long-burst interval of MMS data obtained in the magnetosheath (see Table 2). For this interval, the mean plasma velocity is approximately 230 km s$^{-1}$ and the inter-spacecraft separation is about 27 km, which is below the ion inertial length and corresponds to a few times the electron inertial length. As shown in previous studies (Parashar et al. 2018; Bandyopadhyay et al. 2020a, 2023;

**Table 2.** Description of one selected magnetosheath interval of MMS data. $|\langle \boldsymbol{B} \rangle|$ is the mean magnetic field strength; $\delta B = \sqrt{\langle |\boldsymbol{B}(t) - \langle \boldsymbol{B} \rangle|^2 \rangle}$ is the root-mean-square magnetic fluctuation; $\langle n \rangle$ is the mean plasma density; $\beta_p$ is the proton plasma beta; $d_p$ and $d_e$ are the ion and electron inertial lengths, respectively; and $L$ indicates the mean separation between spacecrafts.

| | $\lvert\langle \boldsymbol{B} \rangle\rvert$ (nT) | $\delta B/\lvert\langle \boldsymbol{B} \rangle\rvert$ | $\langle n_e \rangle$ (cm$^{-3}$) | $\langle n_p \rangle$ (cm$^{-3}$) | $\beta_p$ | $d_p$ (km) | $d_e$ (km) | $L$ (km) |
|---|---|---|---|---|---|---|---|---|
| 2017 Dec 26 06:12:43–06:52:23 | 22.0 | 0.8 | 24.9 | 22.8 | 4.5 | 48 | 1.1 | 27 |

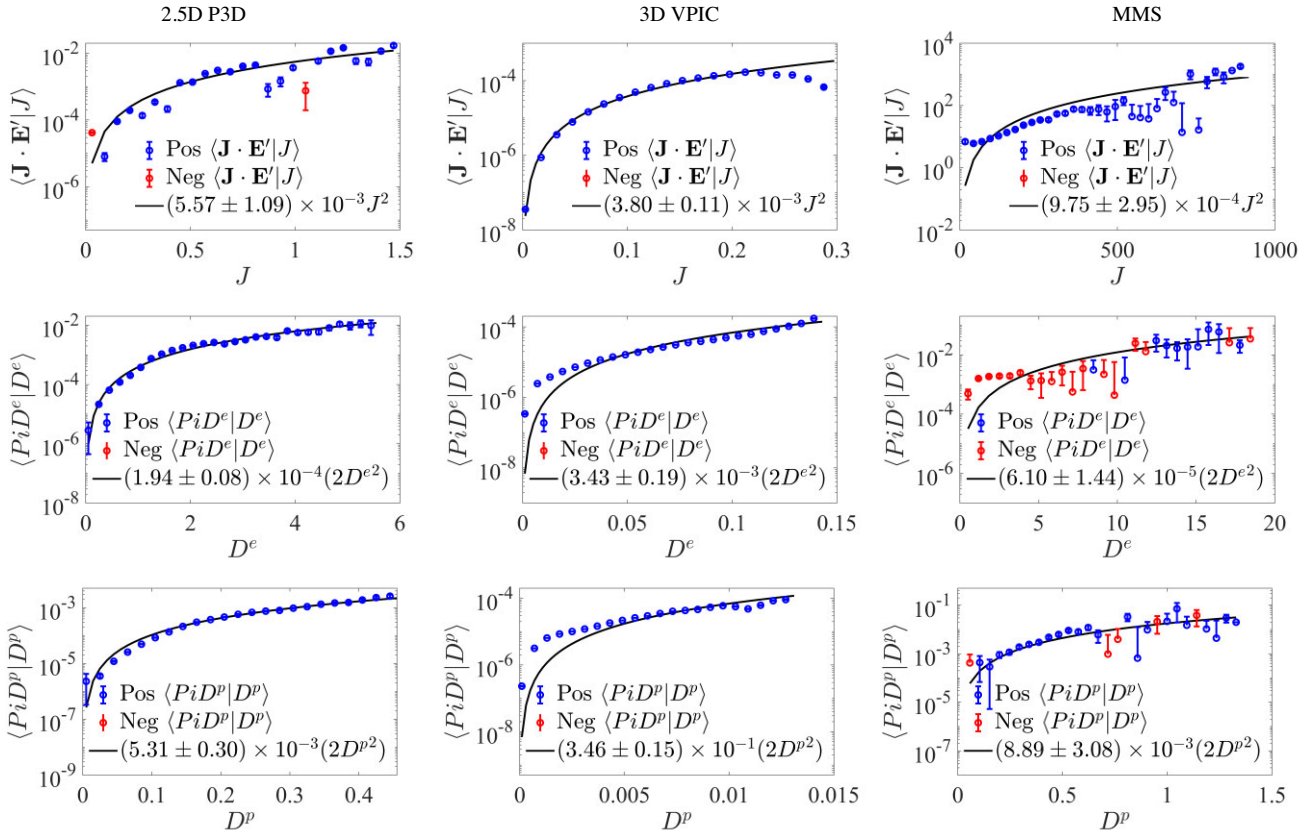


**Figure 1.** Conditional average of (top) the electromagnetic work $\boldsymbol{J} \cdot \boldsymbol{E}'$ with respect to the current density magnitude $J$, and (middle and bottom) Pi-D$^{(\alpha)}$ ($=-\Pi_{ij}^{(\alpha)} D_{ij}^{(\alpha)}$) with respect to the traceless velocity strain rate $D^{(\alpha)} = \sqrt{D_{ij}^{(\alpha)} D_{ij}^{(\alpha)}}$. The error bars are computed from the standard deviation in each bin. The coefficients from least-square fitting, within 95 per cent confidence interval, are also shown. Positive and negative values are identified.

Yang et al. ), this interval exhibits features of well-developed turbulence.

## 4 RESULTS

### 4.1 Kinematic viscosity and magnetic diffusivity

To determine the values of the effective diffusion coefficients, we employ a method based on the recent work of Bandyopadhyay et al. (2023). The basic procedure, for the case of resistivity determination, is to compute $\langle \boldsymbol{J} \cdot \boldsymbol{E}' | J \rangle$, which is the average of the electric work in the electron fluid frame conditioned on the (local) current density magnitude $J = |\boldsymbol{J}|$, and investigate its dependence on $J$. As was noted previously (Wan et al. 2016; Bandyopadhyay et al. 2023), this conditional average is found to follow a curve $\langle \boldsymbol{J} \cdot \boldsymbol{E}' | J \rangle \sim J^2$ to a reasonable degree of accuracy, as shown here in the top row of Fig. 1. The error bars are computed from the standard deviation in each bin. Using this quadratic scaling agreement, we evaluate the constants of proportionality for the two simulations and for the MMS data, thus providing an estimation of the effective resistivity for the respective cases. The functional form of the trend is strongly similar to that of the collisional case, as given in equation (5). This accounts for the heuristic description of the result as 'collisional-like'. These values of 'effective resistivity' $1/\sigma$, within 95 per cent confidence interval, are shown in the legend of Fig. 1 and tabulated in Table 3 in the respective units.

A similar procedure is followed for the the conditional average of the anisotropic part of the pressure–strain interaction, Pi-D$^{(\alpha)}$ ($= -\Pi_{ij}^{(\alpha)} D_{ij}^{(\alpha)}$), which represents the incompressive contribution to the rate of production of thermal energy (Braginskii 1965; Chiuderi & Velli 2015; Yang et al. 2022). This is done separately for electrons and protons. Specifically, we compute the average of electron Pi-D$^e$ conditioned on $D^e \equiv \sqrt{D_{ij}^e D_{ji}^e}$, that is $\langle -\Pi_{ij}^e D_{ij}^e | D^e \rangle$. Recall that the traceless strain rate tensor for the electron fluid velocity is $D_{ij}^e = \frac{1}{2}(\partial_i u_j^e + \partial_j u_i^e) - \frac{1}{3}\delta_{ij} \nabla \cdot \boldsymbol{u}^e$. The general trend is

quite consistent with the collisional scaling in equation (4), as shown in the second row of Fig. 1. Thus, the resulting approximation, that $\langle -\Pi_{ij}^e D_{ij}^e | D^e \rangle \propto (D^e)^2$, is indeed a collisional-like representation of the average results.

**Table 3.** Effective electrical resistivity $1/\sigma$ and effective dynamic viscosity $\mu$ within 95 per cent confidence interval from least-square fitting in Fig. 1, and the corresponding effective kinematic viscosity $\nu = \mu/\rho$ and effective magnetic diffusivity $\eta = 1/(\sigma\mu_0)$. The units are shown enclosed in square brackets and are those that apply to the specific code or data interval.

| Variables | 2.5D P3D | 3D VPIC | MMS |
|---|---|---|---|
| $\frac{1}{\sigma}$ | $(5.57 \pm 1.09) \times 10^{-3}$ [$m_p\,\omega_{cp}\,n_r^{-1}\,e^{-2}$] | $(3.80 \pm 0.11) \times 10^{-3}$ [$m_e\,\omega_{pe}\,n_r^{-1}\,e^{-2}$] | $(9.75 \pm 2.95) \times 10^{-4}$ [mV m nA$^{-1}$] |
| $\eta = \frac{1}{\sigma\mu_0}$ | $(4.43 \pm 0.87) \times 10^{3}$ [$m_p\,\omega_{cp}\,n_r^{-1}\,e^{-2}\,(m\,H^{-1})$] | $(3.02 \pm 0.09) \times 10^{3}$ [$m_e\,\omega_{pe}\,n_r^{-1}\,e^{-2}\,(m\,H^{-1})$] | $(7.76 \pm 2.35) \times 10^{8}$ [m$^2$ s$^{-1}$] |
| $\mu_e$ | $(1.94 \pm 0.08) \times 10^{-4}$ [$m_p\,n_r\,V_{Ar}\,d_p$] | $(3.43 \pm 0.19) \times 10^{-3}$ [$m_e\,n_r\,c\,d_e$] | $(6.10 \pm 1.44) \times 10^{-5}$ [nPa s] |
| $\nu_e = \frac{\mu_e}{\rho_e}$ | $(4.85 \pm 0.20) \times 10^{-3}$ [$V_{Ar}\,d_p$] | $(3.43 \pm 0.19) \times 10^{-3}$ [$c\,d_e$] | $(2.69 \pm 0.64) \times 10^{9}$ [m$^2$ s$^{-1}$] |
| $\mu_p$ | $(5.31 \pm 0.30) \times 10^{-3}$ [$m_p\,n_r\,V_{Ar}\,d_p$] | $(3.46 \pm 0.15) \times 10^{-1}$ [$m_e\,n_r\,c\,d_e$] | $(8.89 \pm 3.08) \times 10^{-3}$ [nPa s] |
| $\nu_p = \frac{\mu_p}{\rho_p}$ | $(5.31 \pm 0.30) \times 10^{-3}$ [$V_{Ar}\,d_p$] | $(6.92 \pm 0.30) \times 10^{-3}$ [$c\,d_e$] | $(2.33 \pm 0.81) \times 10^{8}$ [m$^2$ s$^{-1}$] |

**Table 4.** Effective kinematic viscosity $\nu$ and effective magnetic diffusivity $\eta$ from Table 3 re-expressed in SI units (m$^2$ s$^{-1}$), after mapping the plasma parameters for the MMS interval on to those for the simulations.

| Variables | 2.5D P3D | 3D VPIC | MMS |
|---|---|---|---|
| $\eta$ (m$^2$ s$^{-1}$) | $(2.44 \pm 0.48) \times 10^{7}$ | $(1.21 \pm 0.04) \times 10^{9}$ | $(7.76 \pm 2.35) \times 10^{8}$ |
| $\nu_e$ (m$^2$ s$^{-1}$) | $(2.27 \pm 0.09) \times 10^{7}$ | $(1.13 \pm 0.06) \times 10^{9}$ | $(2.69 \pm 0.64) \times 10^{9}$ |
| $\nu_p$ (m$^2$ s$^{-1}$) | $(2.49 \pm 0.14) \times 10^{7}$ | $(2.28 \pm 0.10) \times 10^{9}$ | $(2.33 \pm 0.81) \times 10^{8}$ |

The analysis for the proton case proceeds in direct analogy to the electron case, with the results shown in the third row of Fig. 1. The conditional average of proton Pi-D$^{\rm p}$ is also found to be well approximated by a fit to a collisional-like scaling, as described in equation (4). That is, $\langle -\Pi^{\rm p}_{ij} D^{\rm p}_{ij} | D^{\rm p}\rangle \propto (D^{\rm p})^2$, where $D^{\rm p}_{ij}$ is the traceless strain rate tensor for the proton fluid velocity and $D^{\rm p} \equiv \sqrt{D^{\rm p}_{ij} D^{\rm p}_{ji}}$.

Fig. 1 also reveals that for these (nearly) collisionless systems $\langle -\Pi^{(\alpha)}_{ij}\, D^{(\alpha)}_{ij} | D^{(\alpha)}\rangle$ is sign-indefinite, especially for the MMS data. This is in contrast to the positive definite collisional dissipation associated with equations (4) and (5). Here, we presume the existence of uniform viscosity and resistivity, and calculate them without taking into account the sign effect. That is, for any negative conditional averages, we use their absolute values when fitting to the collisional scalings. A more careful and refined treatment of the sign effect is deferred to a future study.

The above results, including computations of the effective kinematic viscosity ($\nu = \mu/\rho$) and magnetic diffusivity ($\eta = 1/(\sigma\mu_0)$), are summarized in Table 3. Note that the diffusion coefficients from P3D and VPIC are expressed in the respective code units. To facilitate a direct comparison of the simulation numbers with MMS, we use the plasma properties measured for the MMS interval to convert the diffusion coefficients from code units to SI. That is, to compute the units in P3D, we need to use the proton inertial length $d_{\rm p}$, proton cyclotron frequency $\omega_{\rm cp}$, Alfvén speed $V_{\rm A}$, mean electron number density $\langle n_{\rm e}\rangle$ measured over the MMS interval, and the real-life values of proton mass $m_{\rm p} = 1.67 \times 10^{-27}$ kg and proton charge $e = 1.6 \times 10^{-19}$ C. Similarly, to compute the VPIC units, we use the electron inertial length $d_{\rm e}$, electron plasma frequency $\omega_{\rm pe}$, and mean electron number density $\langle n_{\rm e}\rangle$ from the MMS interval, and the real-life values of electron mass $m_{\rm e}$, proton charge $e$, and speed of light $c$. Finally, the effective kinematic viscosity and effective magnetic diffusivity from the two PIC simulations and the MMS interval are all expressed in SI units, m$^2$ s$^{-1}$ (see Table 4). Note that the viscosity and diffusivity are widely distributed for different data sets, reflecting the physical differences between the simulations and MMS data.

### 4.2 Empirical determination of Reynolds numbers

When the diffusivity is known, a general prescription to obtain a Reynolds number (Re) is to assemble

$$\mathrm{Re} = \frac{\text{speed} \times \text{length}}{\text{diffusivity}}, \tag{11}$$

where the speed and length are those characteristics of the turbulence. The results in the previous section make it possible to compute *effective Reynolds numbers* Re as described in equation (11), since we now have quantitative values for the (effective) diffusivities $\eta$, $\nu_{\rm e}$, and $\nu_{\rm p}$. Choosing the correlation scales for the species velocities, $\lambda_{c,\alpha}$ ($\alpha = e, p$ for electrons and protons, respectively), and magnetic field, $\lambda_{c,b}$, as the characteristic lengths, we may write separate effective Reynolds numbers for the electron and protons, $\mathrm{Re}_{c,\alpha}$, and an effective magnetic Reynolds number, $\mathrm{Re}_{c,b}$, as

$$\mathrm{Re}_{c,\alpha} = \frac{u_\alpha \lambda_{c,\alpha}}{\nu_\alpha}, \tag{12}$$

$$\mathrm{Re}_{c,b} = \frac{u \lambda_{c,b}}{\eta}. \tag{13}$$

Here, $u_\alpha$ are the characteristic fluctuation speeds for each species. For the magnetic Reynolds number, the characteristic speed is denoted by $u$ and there is some flexibility in deciding what value to use for it.

The required values of *correlation scale* can be obtained as follows: The autocorrelation function is defined in the usual way as

$$R(\boldsymbol{r}) = \frac{\langle \boldsymbol{F}(\boldsymbol{x}+\boldsymbol{r}) \cdot \boldsymbol{F}(\boldsymbol{x})\rangle}{\langle \boldsymbol{F}(\boldsymbol{x}) \cdot \boldsymbol{F}(\boldsymbol{x})\rangle}, \tag{14}$$

where $\boldsymbol{F}$ can be either the fluctuation velocity or magnetic field. Note that $R(\boldsymbol{r})$ is a function of lag vector $\boldsymbol{r} = (r_x, r_y, r_z)$. Upon averaging over directions, $R(\boldsymbol{r})$ only depends on lag length $r = |\boldsymbol{r}|$, and $R(r)$ denotes the omnidirectional form of the autocorrelation function. Based on computation of the autocorrelation function, the correlation scale $\lambda_c$ can be defined in several ways. Here, we employ the so-called e-folding method,

$$R(\lambda_c) = 1/\mathrm{e}, \tag{15}$$

where the correlation scale is computed as the scale where the

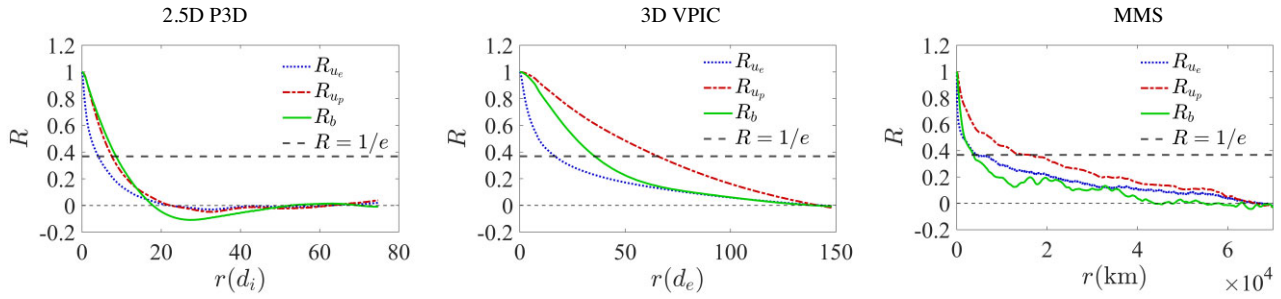


**Figure 2.** Correlation functions for the electron velocity, proton velocity, and magnetic field for the two PIC simulations and the MMS interval.

**Table 5.** Characteristic fluctuation speeds $u$, correlation scales $\lambda_c$, and effective large-scale Reynolds numbers $\mathrm{Re}_c$. Additional $e$, $p$, and $b$ subscripts indicate the quantity for the electrons, protons, or magnetic field, respectively. Here, the characteristic fluctuation speed for protons, $u_\mathrm{p}$, is used to compute the effective magnetic Reynolds number.

| Variables | 2.5D P3D | 3D VPIC | MMS |
|---|---|---|---|
| $u_\mathrm{e} = \sqrt{\langle \boldsymbol{u}_\mathrm{e}^2 \rangle}$ | 0.30 [$V_\mathrm{Ar}$] | 0.055 [c] | 232.8 [km s$^{-1}$] |
| $u_\mathrm{p} = \sqrt{\langle \boldsymbol{u}_\mathrm{p}^2 \rangle}$ | 0.22 [$V_\mathrm{Ar}$] | 0.032 [c] | 242.1 [km s$^{-1}$] |
| $\lambda_{c,\,\mathrm{e}}$ | 4.1 [$d_\mathrm{p}$] | 17 [$d_\mathrm{e}$] | 4380 [km] |
| $\lambda_{c,\,\mathrm{p}}$ | 7.5 [$d_\mathrm{p}$] | 65 [$d_\mathrm{e}$] | 15 990 [km] |
| $\lambda_{c,\,\mathrm{b}}$ | 8.5 [$d_\mathrm{p}$] | 36 [$d_\mathrm{e}$] | 3690 [km] |
| $\mathrm{Re}_{c,\,\mathrm{e}} = u_\mathrm{e}\lambda_{c,\,\mathrm{e}}/\nu_\mathrm{e}$ | 250 | 270 | 380 |
| $\mathrm{Re}_{c,\,\mathrm{p}} = u_\mathrm{p}\lambda_{c,\,\mathrm{p}}/\nu_\mathrm{p}$ | 320 | 300 | 16 610 |
| $\mathrm{Re}_{c,\,\mathrm{b}} = u_\mathrm{p}\lambda_{c,\,\mathrm{b}}/\eta$ | 370 | 310 | 1150 |

autocorrelation function drops to 1/e, on the basis that $\mathrm{e}^{-r/\lambda_c}$ is an adequate approximation for $R(r)$ (Matthaeus et al. 1999; Smith et al. 2018; Wrench et al. 2023).

Fig. 2 shows the results of our correlation analysis of simulation data and MMS observations. These results are employed to extract correlation lengths. The average bulk speed in this MMS interval is approximately $V_\mathrm{SW} = 230$ km s$^{-1}$, which is used to convert temporal scales to spatial scales for the MMS data. Characteristic fluctuation speeds and correlation scales for these three data sets are recorded in Table 5. As the two codes use different normalizations, Table 5 also indicates the relevant normalizing quantities, or units, in square brackets. Together with the (effective) kinematic viscosities and magnetic diffusivities listed in Table 3, these are combined in accordance with equations (12) and (13) to compute the three corresponding effective Reynolds numbers, shown also in Table 5. Notably, for the simulation cases the three Reynolds numbers are all rather similar, whereas for the MMS interval there are sizable differences, which could be attributed to the uncertainties when computing the correlation length.

## 5 DISCUSSION AND CONCLUSIONS

This paper elaborates and extends the previous work by Bandyopadhyay et al. (2023) in which the initial analysis of conditional averages was presented, indicating that a collisional-like dissipation may be present in collisionless plasma, as suggested by consistency of the data with equations (9) and (10). Here, we have quantitatively examined these approximate relations and determined effective viscosities for electrons and protons as well as an effective resistivity. This was carried out separately for two plasma kinetic (PIC) simulations, one 2.5D and one 3D, and for a sample of magnetosheath turbulence data recorded by the MMS mission. Having determined effective diffusion coefficients, and using measured fluctuation speeds and correlation scales, the assembly of effective Reynolds numbers follows directly.

From the effective large-scale Reynolds number, $\mathrm{Re}_c$, relationships involving a plasma equivalent of the Kolmogorov *dissipation scale*, $\lambda_D$, may also be formulated:

$$\frac{\lambda_c}{\lambda_D} = C_\epsilon^{1/4}\mathrm{Re}_c^{3/4}, \tag{16}$$

where $C_\epsilon$ is the dimensionless dissipation rate. This relation is formulated based on the classic development in hydrodynamic turbulence theory (Kolmogorov 1941a, b; Batchelor 1970), and may be used in several ways.

One might substitute measured correlation scales $\lambda_c$ and effective Reynolds numbers $\mathrm{Re}_c$ into the formula to extract an estimate of the dissipation scale $\lambda_D$. Alternatively, one might assume, as has been done previously, that the dissipation scale in a plasma such as solar wind, corresponds to the upper end of the inertial range. Then, if the value of $\lambda_D$ is taken to be, for example, the ion (or electron) inertial length $d_\mathrm{p}$ (or $d_\mathrm{e}$), equation (16) may be construed as providing another alternative estimate of (effective) Reynolds number. There are also other approaches for estimating the dissipation scale. For example, if the cascade rate $\epsilon$ is known and an effective viscosity is available, hydrodynamic turbulence theory provides the Kolmogorov-style estimate $\lambda_D = (\nu^3/\epsilon)^{1/4}$.

The Reynolds numbers determined here are roughly consistent with reasonable estimates of the corresponding dissipation scales, through the formulation given by equation (16). For example, substituting the proton Reynolds number $\mathrm{Re}_{c,\,p} = 320$ for the 2.5D simulations into equation (16) and using a value $C_\epsilon = (2 \times 0.5)/(9\sqrt{3})$ (as in, e.g. Linkmann, Berera & Goldstraw 2017; Bandyopadhyay et al. 2018; Li et al., in preparation; Wrench et al. 2023) and the measured correlation scale $\lambda_{c,\,\mathrm{p}} = 7.5\,d_\mathrm{p}$, the relation equation (16) gives $\lambda_D \sim 0.2\,d_\mathrm{p}$, which is not an unreasonable estimation. For the MMS data, the same line of analysis leads to the estimate $\lambda_D \sim$ 22 km. This too is a reasonable estimate for the dissipation scale in the magnetosheath, where for this interval the value of $d_\mathrm{p}$ is 48 km (see Table 2). In fact, there are several other ways to combine the above values of Reynolds numbers and measured parameters to examine consistency with traditional estimates. All the combinations we have tried provide reasonable answers, such as values of $\lambda_D$ that are deemed reasonable given the findings from simulations and other observations that spectral steepening usually occurs near $d_\mathrm{p}$. However, no firm guidance is available providing a more detailed picture of a scale at which electron and proton dissipation become dominant or 'turn on' relative to each other (see e.g. Yang et al. 2022).

In identifying length-scales associated with collisionless dissipation, it is of significance that kinetic activity including conversion

of turbulence energy into internal energy (i.e. heating) is found in plasma simulation to be localized in coherent structures that are typically several ion inertial lengths (Greco et al. 2012; Servidio et al. 2012) in thickness at order one plasma beta, but with substructure down to electron scales (Karimabadi et al. 2013); see also discussion in Section 2.3. The same characteristic scale is found to be associated with the 'break' in the solar wind magnetic spectrum associated with termination of the inertial range (Chen et al. 2014), and the limit of the range of applicability of standard MHD in favour of including more complex effects such as Hall MHD (Sonnerup 1979; Shay et al. 1998). The association of this same scale – a few ion inertial lengths – with the onset of the pressure–strain interaction lends credence to a view that these are the scales that signal the onset of collisionless dissipation (Matthaeus et al. 2020). It seems reasonable to suppose that it is the first kinetic scale encountered by the cascade that triggers the onset of collisionless effects. This may select, for example, depending on plasma beta, either ion inertial scale or cyclotron radius as the scale of interest (Chen et al. 2014).

Another interesting aspect of the present results is the size of the (effective) magnetic Prandtl number $Pm$, generally defined as the ratio of kinematic viscosity $\nu$ to magnetic diffusivity $\eta$. Here, examining the values of the effective magnetic diffusivity and two viscosities stated in Table 4, we see that the magnetic Prandtl number estimates from both simulation results are near unity. For the MMS data, the value is only moderately away from unity. The significance of this is that when $Pm$ greatly differs from unity, different regimes of MHD scale behaviour become possible (Cho, Lazarian & Vishniac 2002; Ponty et al. 2005; Sahoo, Perlekar & Pandit 2011). In particular, in such cases the inertial ranges in magnetic field and velocity field can develop very different bandwidths. A value of $Pm$ near unity is consistent with the usual finding of 'Alfvénic' turbulence in which there is order one equipartition of magnetic and velocity field energy in their respective inertial ranges over very similar ranges of wavenumber.

In this work, we have assumed that the effective viscosity and resistivity are spatially uniform scalars. This simplification facilitates analysis of the simulation and MMS data sets. This approach is also motivated by earlier results seen in the conditional statistics reported in Yang et al. (2017b) and Bandyopadhyay et al. (2023). The more general situation of non-uniform and anisotropic (tensor) effective viscosity and resistivity is possible, and in fact likely, as these coefficients should be dependent on current density (Bessho & Bhattacharjee 2010, 2012; Selvi et al. 2023) and velocity shear (Del Sarto et al. 2016; Del Sarto & Pegoraro 2018). For example, in collisionless reconnection, Selvi et al. (2023) and Bessho & Bhattacharjee (2010, 2012) propose a kinetic physics-motivated model for non-uniform effective resistivity that is negligible on global scales and becomes significant only locally near X-points.

Furthermore, the assumption of scalar coefficients is also unlikely to be sufficiently general for the typical anisotropies expected to occur in space plasmas in the presence of a magnetic field. It turns out that in a magnetized plasma, both the pressure tensor $\boldsymbol{P}$ and the traceless strain rate tensor $\boldsymbol{D}$ are highly anisotropic (Oughton et al. 2015; Del Sarto et al. 2016; Yang et al. 2023). Also anisotropic is the electric work $\boldsymbol{J}\cdot\boldsymbol{E}$, whose parallel and perpendicular elements (with respect to the mean magnetic field) might contribute differently to particle energization in, for example, reconnection zones (Dahlin, Drake & Swisdak 2014; Li et al. 2015). The anisotropy is intimately related to the structure of potential closure models, if any exist in collisionless plasmas, in which dissipation coefficients are more plausibly treated as components of second-rank tensors (Thompson 1961; Braginskii 1965; Macmahon 1965; Smolyakov 1998). Therefore, a more complete model for effective viscosity and resistivity in collisionless plasma should allow for both spatial non-uniformity and (non-scalar) tensor structure.

We remark that although the classical collisional diffusivity must obviously be absent in collisionless plasmas, a number of previous works have none the less attempted to write approximate expressions for effective diffusion coefficients in collisionless plasma. Possible candidates that act as effective collisions include wave–particle interactions (Graham et al. 2022), pitch angle scattering (Earl, Jokipii & Morfill 1988; Zank et al. 2014), stochastic field line effects (Coroniti & Eviatar 1977; Lazarian & Vishniac 1999), and other kinetic mechanisms. In particular, viscosity and resistivity have been estimated based on various approximations; for the present, we leave aside the estimation of other transport coefficients such as heat conduction (Hollweg 1976; Riquelme, Quataert & Verscharen 2016). Previous attempts to calculate anomalous resistivity have been made in collisionless reconnection to sustain reconnection electric field (Coroniti & Eviatar 1977; Lazarian & Vishniac 1999; Bessho & Bhattacharjee 2010, 2012; Graham et al. 2022; Selvi et al. 2023). In the case of hyper-resistivity, the non-ideal electric field in collisionless reconnection is also found to be consistent with the dissipation due to anomalous electron viscosity (Strauss 1986; Fujimoto & Sydora 2021, 2023). A collisional-like viscosity is already present in earlier studies, such as gyroviscosity (Thompson 1961; Roberts & Taylor 1962; Macmahon 1965; Smolyakov 1998), cosmic ray viscosity (Earl et al. 1988), and plasma viscosity (Kaufman 1960). Viscous effects are often estimated by consideration of the MHD-scale cascade and its implications for pressure anisotropies (Quataert & Gruzinov 1999; Sharma et al. 2007; Verma 2019). Considerations of pressure anisotropy (Kasper, Lazarus & Gary 2002; Matteini et al. 2007), and linear instabilities that drive it, can be employed to develop theories for effective viscosity. This may be particularly effective when combined with exact results from Vlasov–Maxwell theory, such as dissipation through the pressure–strain interaction (Yang et al. 2017a). Such considerations have motivated more elaborate approximate models for effective viscosity based on pressure anisotropy in the simplified Chew-Goldberger-Low (CGL) model (Arzamasskiy et al. 2023; Squire et al. 2023). Valuable insights are obtained from models of this type, especially with regard to extrapolations to extreme values of plasma $\beta$ that can be relevant to astrophysical systems (Howes 2010; Kawazura, Barnes & Schekochihin 2019; Roy et al. 2022).

Finally, we recall that several additional relationships may be adapted from classical turbulence theory to provide alternative estimates for Reynolds numbers and diffusivities. One possibility is to base measurements on the Taylor microscale $\lambda_{\mathrm{T}}$, which can be related directly to the second derivative of the autocorrelation function evaluated at the origin (e.g. Batchelor 1970; Pope 2000). Up to order unity constants, $\lambda_{\mathrm{T}} = [-R'(0)]^{-1/2}$, where we have in mind that $R(r)$ is the direction-averaged correlation function of, say, the magnetic field, as in equation (14). Then, one can show that an estimate of the effective Reynolds number can be written as $\mathrm{Re} = (\lambda_c/\lambda_{\mathrm{T}})^2/C_\epsilon$ (e.g. Wrench et al. 2023). This quantity is measurable when high-resolution data are available, and may be further developed into an estimate of the effective viscosity, as shown by Bandyopadhyay et al. (2020b). The above relationships should be viewed as semi-empirical and, while motivated by theory, should not be treated as exact in any sense, since the underlying theories are mainly hydrodynamic (and collisional) and usually founded on simple assumptions of rotational symmetry or incompressibility.

Based on the above results and given the unique nature of the analysis developed so far, we conclude that the present approach

to quantifying collisional-like dissipation in collisionless plasma turbulence warrants further investigation. Already we have seen herein that examination of conditional averages of pressure–strain interaction and electric work, which themselves are exact statements of energy conversion rates, provides a basis for finding effective diffusion coefficients. With apparently reasonable values of (effective) Reynolds numbers, viscosities, and resistivities in hand, the door is opened to examining a class of relationships that may help bring turbulence theory concepts into greater contact with turbulent plasma, as we have described above. There is clearly much more to do in the complex subject of plasma turbulence, and this work offers a small step in a possibly useful direction.

## ACKNOWLEDGEMENTS

This research was supported in part by the MMS Theory and Modeling grant 80NSSC19K0565 at Delaware, and by NSFDOE grant PHYS-2108834 at Delaware, and NASA Heliospheric GI grant no. 80NSSC21K0739 and NASA grant no. 80NSSC21K1458 at Princeton University, and a subcontract SUB0000317 to Delaware. This research was also supported by the International Space Science Institute (ISSI) in Bern, through ISSI International Team project #556 (Cross-scale energy transfer in space plasmas). MAS acknowledges support from NASA LWS grant 80NSSC20K0198. We would like to acknowledge high-performance computing support from Cheyenne (doi:10.5065/D6RX99HX) and Derecho (https://doi.org/10.5065/qx9a-pg09) provided by NCAR's Computational and Information Systems Laboratory, sponsored by the National Science Foundation. This research also used resources of the National Energy Research Scientific Computing Center, which is supported by the Office of Science of the U.S. Department of Energy under Contract No. DE-AC02-05CH11231. We are particularly grateful to Sylvie Yang Jin (金浠言) for cooperation and assisting the lead author in completing this research.

## DATA AVAILABILITY

This study used Level 2 FPI and FIELDS data according to the guidelines set forth by the MMS instrumentation team. The data that support the findings of this study are openly available in MMS Science Data Center (SDC) at https://lasp.colorado.edu/MMS/sdc/. Other reasonable requests for sharing of the metadata regarding computational runs, custom simulation codes, and documentation will generally be honoured.

## REFERENCES

Alexandrova O., Saur J., Lacombe C., Mangeney A., Mitchell J., Schwartz S. J., Robert P., 2009, Phys. Rev. Lett., 103, 165003
Andrés N., Sahraoui F., Galtier S., Hadid L. Z., Ferrand R., Huang S. Y., 2019, Phys. Rev. Lett., 123, 245101
Arzamasskiy L., Kunz M. W., Squire J., Quataert E., Schekochihin A. A., 2023, Phys. Rev. X, 13, 021014
Bandyopadhyay R., Oughton S., Wan M., Matthaeus W. H., Chhiber R., Parashar T. N., 2018, Phys. Rev. X, 8, 041052
Bandyopadhyay R. et al., 2020a, Phys. Rev. Lett., 124, 255101
Bandyopadhyay R. et al., 2020b, ApJ, 899, 63
Bandyopadhyay R. et al., 2023, Phys. Plasmas, 30, 080702
Banerjee S., Andrés N., 2020, Phys. Rev. E, 101, 043212
Barbhuiya M. H., Cassak P. A., 2022, Phys. Plasmas, 29, 122308
Batchelor G. K., 1970, The Theory of Homogeneous Turbulence. Cambridge Univ. Press, Cambridge
Bessho N., Bhattacharjee A., 2010, Phys. Plasmas, 17, 102104
Bessho N., Bhattacharjee A., 2012, ApJ, 750, 129
Bowers K. J., Albright B. J., Yin L., Bergen B., Kwan T. J. T., 2008, Phys. Plasmas, 15, 055703
Braginskii S. I., 1965, Rev. Plasma Phys., 1, 205
Bruno R., Carbone V., 2013, Living Rev. Sol. Phys., 10, 2
Burch J. L. et al., 2016, Science, 352, aaf2939
Cassak P. A., Barbhuiya M. H., 2022, Phys. Plasmas, 29, 122306
Cassak P. A., Barbhuiya M. H., Weldon H. A., 2022, Phys. Plasmas, 29, 122307
Chandran B. D. G., Li B., Rogers B. N., Quataert E., Germaschewski K., 2010, ApJ, 720, 503
Chapman S., Cowling T. G., 1939, The Mathematical Theory of Non-uniform Gases: An Account of the Kinetic Theory of Viscosity, Thermal Conduction and Diffusion in Gases. Cambridge Univ. Press, Cambridge
Chasapis A. et al., 2018, ApJ, 856, L19
Chen C. H. K., Leung L., Boldyrev S., Maruca B. A., Bale S. D., 2014, Geophys. Res. Lett., 41, 8081
Chiuderi C., Velli M., 2015, Basics of Plasma Astrophysics. Springer-Verlag, Berlin
Cho J., Lazarian A., Vishniac E. T., 2002, ApJ, 564, 291
Chuychai P., Weygand J. M., Matthaeus W. H., Dasso S., Smith C. W., Kivelson M. G., 2014, J. Geophys. Res., 119, 4256
Coleman P. J., 1968, ApJ, 153, 371
Coroniti F. V., Eviatar A., 1977, ApJS, 33, 189
Cuesta M. E., Parashar T. N., Chhiber R., Matthaeus W. H., 2022, ApJS, 259, 23
Dahlin J. T., Drake J. F., Swisdak M., 2014, Phys. Plasmas, 21, 092304
de Kármán T., Howarth L., 1938, Proc. R. Soc. A, 164, 192
Del Sarto D., Pegoraro F., 2018, MNRAS, 475, 181
Del Sarto D., Pegoraro F., Califano F., 2016, Phys. Rev. E, 93, 053203
Dmitruk P., Matthaeus W. H., Seenu N., 2004, ApJ, 617, 667
Earl J. A., Jokipii J. R., Morfill G., 1988, ApJ, 331, L91
Ergun R. E. et al., 2016, Space Sci. Rev., 199, 167
Franci L., Landi S., Matteini L., Verdini A., Hellinger P., 2016, ApJ, 833, 91
Fujimoto K., Sydora R. D., 2021, ApJ, 909, L15
Fujimoto K., Sydora R. D., 2023, Phys. Plasmas, 30, 022106
Graham D. B. et al., 2017, Phys. Rev. Lett., 119, 025101
Graham D. et al., 2022, Nat. Commun., 13, 1
Greco A., Valentini F., Servidio S., Matthaeus W. H., 2012, Phys. Rev. E, 86, 066405
Hadid L. Z., Sahraoui F., Galtier S., 2017, ApJ, 838, 9
Hellinger P., Montagud-Camps V., Franci L., Matteini L., Papini E., Verdini A., Landi S., 2022, ApJ, 930, 48
Hollweg J. V., 1976, J. Geophys. Res., 81, 1649
Hossain M., Gray P. C., Pontius D. H.,, Jr, Matthaeus W. H., Oughton S., 1995, Phys. Fluids, 7, 2886
Howes G. G., 2010, MNRAS, 409, L104
Howes G. G., Dorland W., Cowley S. C., Hammett G. W., Quataert E., Schekochihin A. A., Tatsuno T., 2008, Phys. Rev. Lett., 100, 065004
Karimabadi H. et al., 2013, Phys. Plasmas, 20, 012303
Kasper J. C., Lazarus A. J., Gary S. P., 2002, Geophys. Res. Lett., 29, 20
Kaufman A. N., 1960, Phys. Fluids, 3, 610
Kawazura Y., Barnes M., Schekochihin A. A., 2019, Proc. Natl. Acad. Sci. USA, 116, 771
Kiyani K. H., Osman K. T., Chapman S. C., 2015, Phil. Trans. R. Soc. A, 373, 20140155
Kolmogorov A. N., 1941a, Dokl. Akad. Nauk SSSR, 30, 301
Kolmogorov A. N., 1941b, C. R. Acad. Sci. U.R.S.S., 32, 16
Lazarian A., Vishniac E. T., 1999, ApJ, 517, 700
Leamon R. J., Smith C. W., Ness N. F., Matthaeus W. H., Wong H. K., 1998, J. Geophys. Res., 103, 4775
Li X., Guo F., Li H., Li G., 2015, ApJ, 811, L24
Linkmann M., Berera A., Goldstraw E. E., 2017, Phys. Rev. E, 95, 013102
Macmahon A., 1965, Phys. Fluids, 8, 1840
Markovskii S. A., Vasquez B. J., Smith C. W., Hollweg J. V., 2006, ApJ, 639, 1177
Marsch E., 2006, Living Rev. Sol. Phys., 3, 1

Marshall W., 1960, The Kinetic Theory of an Ionized Gas, Atomic Energy Research Establishment, Harwell, Berkshire, UK
Matteini L., Landi S., Hellinger P., Pantellini F., Maksimovic M., Velli M., Goldstein B. E., Marsch E., 2007, Geophys. Res. Lett., 34, L20105
Matthaeus W. H., Zank G. P., Smith C. W., Oughton S., 1999, Phys. Rev. Lett., 82, 3444
Matthaeus W. H., Dasso S., Weygand J. M., Milano L. J., Smith C. W., Kivelson M. G., 2005, Phys. Rev. Lett., 95, 231101
Matthaeus W. H., Weygand J. M., Chuychai P., Dasso S., Smith C. W., Kivelson M. G., 2008, ApJ, 678, L141
Matthaeus W. H., Yang Y., Wan M., Parashar T. N., Bandyopadhyay R., Chasapis A., Pezzi O., Valentini F., 2020, ApJ, 891, 101
Osman K. T., Matthaeus W. H., Greco A., Servidio S., 2011, ApJ, 727, L11
Oughton S., Matthaeus W. H., Wan M., Osman K. T., 2015, Phil. Trans. R. Soc. A, 373, 20140152
Parashar T. N., Matthaeus W. H., 2016, ApJ, 832, 57
Parashar T. N., Servidio S., Shay M. A., Breech B., Matthaeus W. H., 2011, Phys. Plasmas, 18, 092302
Parashar T. N. et al., 2018, Phys. Rev. Lett., 121, 265101
Parashar T. N., Cuesta M., Matthaeus W. H., 2019, ApJ, 884, L57
Perri S. et al., 2020, J. Plasma Phys., 86, 905860108
Phillips C., Bandyopadhyay R., McComas D. J., 2022, ApJ, 933, 33
Politano H., Pouquet A., 1998, Geophys. Res. Lett., 25, 273
Pollock C. et al., 2016, Space Sci. Rev., 199, 331
Ponty Y., Mininni P. D., Montgomery D. C., Pinton J.-F., Politano H., Pouquet A., 2005, Phys. Rev. Lett., 94, 164502
Pope S. B., 2000, Turbulent Flows. Cambridge Univ. Press, Cambridge
Quataert E., Gruzinov A., 1999, ApJ, 520, 248
Retinò A., Sundkvist D., Vaivads A., Mozer F., André M., Owen C. J., 2007, Nat. Phys., 3, 236
Riquelme M. A., Quataert E., Verscharen D., 2016, ApJ, 824, 123
Roberts K. V., Taylor J. B., 1962, Phys. Rev. Lett., 8, 197
Roy S. et al., 2022, ApJ, 941, 137
Roytershteyn V., Karimabadi H., Roberts A., 2015, Phil. Trans. R. Soc. A, 373, 20140151
Russell C. T. et al., 2016, Space Sci. Rev., 199, 189
Sahoo G., Perlekar P., Pandit R., 2011, New J. Phys., 13, 013036
Sahraoui F., Goldstein M. L., Robert P., Khotyaintsev Y. V., 2009, Phys. Rev. Lett., 102, 231102
Selvi S., Porth O., Ripperda B., Bacchini F., Sironi L., Keppens R., 2023, ApJ, 950, 169
Servidio S., Valentini F., Califano F., Veltri P., 2012, Phys. Rev. Lett., 108, 045001
Sharma P., Quataert E., Hammett G., Stone J. M., 2007, ApJ, 667, 714
Shay M. A., Drake J. F., Denton R. E., Biskamp D., 1998, J. Geophys. Res., 103, 9165
Smith C. W., Hamilton K., Vasquez B. J., Leamon R. J., 2006, ApJ, 645, L85
Smith C. W., Vasquez B. J., Coburn J. T., Forman M. A., Stawarz J. E., 2018, ApJ, 858, 21
Smolyakov A. I., 1998, Can. J. Phys., 76, 321
Sonnerup B., 1979, in Lanzerotti L. J., Kennel C. F., Parker E. N., eds, Solar System Plasma Physics, Vol. III. North-Holland Publishing Company, Amsterdam, p. 45
Sorriso-Valvo L. et al., 2007, Phys. Rev. Lett., 99, 115001
Squire J., Kunz M., Arzamasskiy L., Johnston Z., Quataert E., Schekochihin A., 2023, J. Plasma Phys., 89, 905890417
Strauss H., 1986, Phys. Fluids, 29, 3668
Thompson W., 1961, Rep. Prog. Phys., 24, 363
Verma M. K., 1996, J. Geophys. Res., 101, 27543
Verma M. K., 2019, Eur. Phys. J. B, 92, 190
Verniero J. L. et al., 2020, ApJS, 248, 5
Wan M., Oughton S., Servidio S., Matthaeus W. H., 2012, J. Fluid Mech., 697, 296
Wan M., Matthaeus W. H., Roytershteyn V., Parashar T. N., Wu P., Karimabadi H., 2016, Phys. Plasmas, 23, 042307
Wrench D., Parashar T. N., Oughton S., De Lange K., Frean M., 2024, ApJ, 961, 182
Yang Y. et al., 2017a, Phys. Plasmas, 24, 072306
Yang Y. et al., 2017b, Phys. Rev. E, 95, 061201
Yang Y., Matthaeus W. H., Roy S., Roytershteyn V., Parashar T. N., Bandyopadhyay R., Wan M., 2022, ApJ, 929, 142
Yang Y. et al., 2023, ApJ, 944, 148
Zank G., Hunana P., Mostafavi P., Goldstein M., 2014, ApJ, 797, 87
Zank G. P., Adhikari L., Hunana P., Shiota D., Bruno R., Telloni D., 2017, ApJ, 835, 147
Zeiler A., Biskamp D., Drake J. F., Rogers B. N., Shay M. A., Scholer M., 2002, J. Geophys. Res., 107, 1230
Zenitani S., Hesse M., Klimas A., Kuznetsova M., 2011, Phys. Rev. Lett., 106, 195003

This paper has been typeset from a TEX/LATEX file prepared by the author.